Electron Transport in Dye-Sensitized Solar Cells Based on ZnO Nanotubes: Evidence for Highly Efficient Charge Collection and Exceptionally Rapid Dynamics†

Alex B. F. Martinson,[⊥,‡] Márcio S. Góes,[§,||] Francisco Fabregat-Santiago,[§] Juan Bisquert,*[,§] Michael J. Pellin,[⊥,‡] and Joseph T. Hupp*[,⊥,‡]

Department of Chemistry and Argonne-Northwestern Solar Energy Research (ANSER) Center, Northwestern University, 2145 Sheridan Road, Evanston, Illinois 60208, Materials Science Division, Argonne National Laboratory, 9700 South Cass Avenue, Argonne, Illinois 60439, Departament de Física, Universitat Jaume I, Av. Sos Baynat, s/n, 12071 Castelló, Spain, and Departamento de Físico-Química, Instituto de Química de Araraquara, Universidade Estadual Paulista, R. Prof. Francisco Degni s/n, 14800-900 Araraquara SP, Brazil

Received: November 26, 2008; Revised Manuscript Received: December 19, 2008

Dye-sensitized solar cells based on ordered arrays of polycrystalline ZnO nanotubes, 64 μm in length, are shown to exhibit efficient electron collection over the entire photoanode array length. Electrochemical impedance spectroscopy, open-circuit photovoltage decay analysis, and incident-photon-to-current efficiency spectra are used to quantify charge transport and lifetimes. Despite the relatively thick photoanode, the charge extraction time is found to be faster than observed in traditional TiO_2 nanoparticle photoanodes. If the extraction dynamics are interpreted as diffusive, effective electron diffusion coefficients of up to 0.4 $cm^2\ s^{-1}$ are obtained, making these pseudo-1D photoanodes the fastest reported for an operating DSC to date. Rapid electron collection is of practical significance because it should enable alternative redox shuttles, which display relatively fast electron-interception dynamics, to be employed without significant loss of photocurrent.

Introduction

O'Regan and Graetzel's 1991 report on dye-sensitized solar cells (DSCs) that combined high area, nanoparticulate photoelectrodes with a slow redox shuttle (iodide/triiodide) constituted a remarkable performance and design breakthrough. These devices, and the most promising variants explored since then, have been characterized by exceptional monochromatic incident photon-to-current efficiencies (IPCEs).[1,2] As summarized by eq 1

$$\mathrm{IPCE} = \eta_{\mathrm{LH}} \cdot \eta_{\mathrm{CS}} \cdot \eta_{\mathrm{CC}} \quad (1)$$

the IPCE can be viewed as a collective measure of the efficiencies (η) of three key cell processes: light harvesting (LH), separation of opposing charges (CS), and collection of the charges (CC) at the appropriate electrodes. That IPCEs approach unity at the peak absorbance in the most efficient DSCs implies that nearly every photon of this wavelength is harvested ($\eta_{\mathrm{LH}} \sim 1$) by the moderately high extinction dyes bound to the high surface area electrodes. Furthermore, it must be the case that nearly every photoexcited dye successfully injects an electron into the semiconductor network ($\eta_{\mathrm{CS}} \sim 1$). Finally, at least at short circuit, the injected electron passes through the nanoparticle network to be collected at the transparent electrode without recombining with the oxidized dye or being intercepted by adjacent oxidizing equivalents (I_3^-) in solution ($\eta_{\mathrm{CC}} \sim 1$).

It has been noted that of particular improbability in this electrochemical system is the high η_{CC}, considering the millisecond time scale over which electrons traverse the photoanode in such close proximity to oxidizing species.[3,4] For comparison, carriers cross silicon photovoltaics in tens of microseconds,[5] while charge collection in efficient organic photovoltaics occurs on the tens of nanoseconds time scale.[6] Indeed, it is this relatively slow electron collection in DSCs that is responsible for the very small number of feasible DSC redox shuttles discovered to date. Due to a simple kinetic competition between electron collection and capture (by I_3^-), IPCEs are dramatically reduced when electron recombination is accelerated (lifetime shortened), an effect which has been modeled in detail.[7−9] It is not surprising then, that several novel photoanode architectures with the prospect of rapid charge collection have recently been explored.[4,10−13] Access to these architectures has been facilitated by several attractive fabrication strategies, among them (a) surfactant-controlled crystallization,[10,14] (b) controlled film corrosion,[15] and (c) templated atomic-layer deposition (ALD).[11,16−24] Pseudo 1-D nanostructures, particularly with single or polycrystalline domains, are especially interesting since electrons traveling through the nanoparticle semiconductors are believed to move under diffusive control.[25]

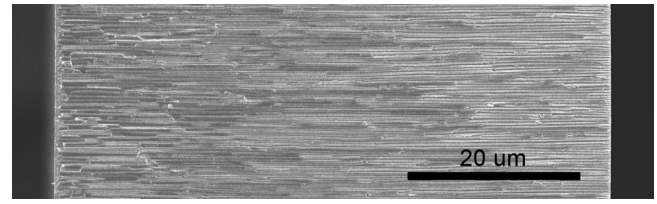

Figure 1. Cross-sectional SEM image of an anodic aluminum oxide template coated with ZnO by atomic layer deposition. On average, the pores of the 64 μm thick membranes are 215 nm in diameter and spaced 330 nm on center.

Here we quantify the characteristic conductivity and capacitance of the photoanodes, Figure 1, in assembled ZnO nanotube DSCs via electrochemical impedance spectroscopy (EIS). The charge lifetime, τ_n, and charge extraction time, τ_d, are derived from equivalent circuit analysis along with an estimation of the charge extraction length, L_n. Rapid screening of several redox shuttle solutions by photovoltage decay analysis under open-

† Part of the "George C. Schatz Festschrift".

* To whom correspondence should be addressed. E-mail: j-hupp@northwestern.edu, bisquert@fca.uji.es.

⊥ Northwestern University.

‡ Argonne National Laboratory.

§ Universitat Jaume I.

|| Universidade Estadual Paulista.

10.1021/jp810406q CCC: $40.75
Published on Web 02/10/2009

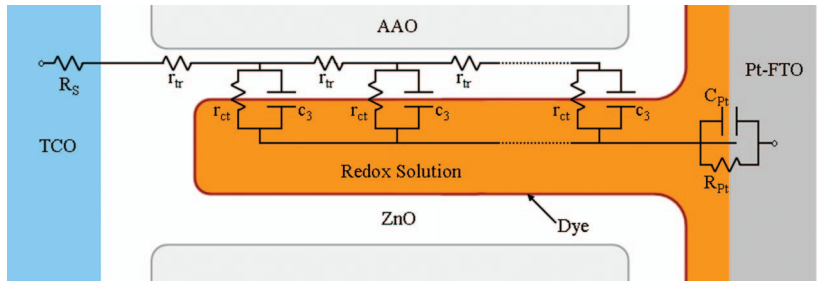

Figure 2. Equivalent circuit to which impedance spectra are fit overlays a highly idealized photoanode schematic. Equivalent circuit elements overlay the geometrically appropriate interface. Note that the schematic is not drawn to scale and that the aspect ratio of the nanotubes (~3 as shown here) is experimentally much larger (~400, see Figure 1) in order to achieve reasonable light-harvesting efficiency.

circuit conditions corroborates τ_n and illustrates the opportunity for efficient charge collection under accelerated recombination conditions. Analysis of IPCEs under increasing [I_3^-] (faster recombination) supports the hypothesis that photogenerated electrons are efficiently collected, despite the substantial length of the nanotubes that comprise the array. Based on evidence of a diffusive transport mechanism, these measurements reveal the fastest electron collection of any DSC photoanode to date.

Experimental Methods

Devices were constructed similarly to those previously reported.[11] Briefly, commercial anodic alumina oxide (AAO) membranes (Whatman 13, 0.02 μm) were uniformly and conformally coated with 16 nm of polycrystalline ZnO via atomic layer deposition (ALD) at 150 °C. Prior to deposition of the transparent conducting oxide (TCO), the photoanodes were fired in air at 450 °C for 30 min to increase crystallinity. A Surlyn hot melt spacer frame (25 μm, Solaronix) was sandwiched between the photoanode and platinized fluorine-doped tin oxide (FTO) electrode at 80 °C. The iodide-based redox shuttle solution was composed of 0.5 M LiI, 0.5 M *tert*-butylpyridine, and 0.05 M I_2 in 3-methoxypropionitrile (3-MPN). For experiments with increasing [I_3^-], additional LiI and I_2 were added with the assumption that their reaction goes nearly to completion.

Electrochemical impedance spectroscopy (EIS) was performed with a Solartron 1260A frequency response analyzer coupled to a Solartron 1286 electrochemical interface. Cells were measured in two-electrode configuration in the dark with 10 mV AC perturbation over a frequency range of 60 mHz to 60 kHz. Additional three-electrode measurements were performed in an inert electrolyte solution of tetra-*n*-butylammonium hexafluorophosphate ($TBAPF_6$) (0.1 M in 3-MPN) using Ag/$AgNO_3$ (10 mM in acetonitrile) as reference, platinum as counter, and the ZnO nanotube array without dye loading as working electrode. In this case, a PGSTAT-30 potentiostat with frequency analysis module (FRA) from Autolab was used to obtain EIS spectra. Again, the amplitude of the AC signal used was 20 mV, and frequency was varied between 5 mHz and 400 kHz. Zview equivalent circuit modeling software was used to fit the data by utilizing built-in extended element (DX type 11-Bisquert #2), which allows for transmission line modeling (see Figure 2).

Photovoltage decays were measured under open-circuit voltage conditions with a CH Instruments 1202 potentiostat. Monochromatic illumination onto the photoanode side of the device for IPCE analysis was performed through the excitation monochromator of a Jobin-Yvon fluorescence spectrometer with 13 nm bandpass. Photocurrents were collected under short-circuit conditions in 10 nm increments. The η_{LH} of completed ZnO nanorod array DSC was derived from transmission and reflectivity measurements of the isopropanol-wetted photoanode before and after dye loading with a UV−vis−NIR spectrophotometer (Varian Cary 5000) equipped with an integrating sphere accessory (DRA-2500). A correction was made for the reflectance of the photoanode after dye-loading but not the absorbance due to the anterior TCO.

Results and Discussion

A. Electrochemical Impedance Spectroscopy. EIS is an effective technique for elucidating the competition between electron interception (typically by I_3^-) and diffusion to the current collector (generally a TCO).[26−28] As a useful point of reference, the most efficient (i.e., 10 to 11% power efficient) DSCs to date have been characterized using EIS.[4] Similar to this and other literature reports, impedance spectra were fit to a geometrically appropriate equivalent circuit,[29] Figure 2. The most detailed literature models may be simplified for the system described here due to the absence of exposed TCO and the restriction to low current conditions in which electrolyte diffusion impedance (Z_d) is vanishingly small. It should be noted that in contrast to traditional nanoparticle photoanodes, electrolyte communication with the TCO is inhibited by the architecture of the photoelectrode itself. (Briefly, the AAO-based template features channels that taper, on one end only, to ~10 nm radius. Deposition of 16 nm of ZnO fully closes the channels.)

A representative Nyquist plot, Figure 3, shows characteristic features of the ZnO nanotube DSC device impedance. In accordance with other DSC impedances, the primary feature (a low frequency semicircle) is assigned to the resistance to charge transfer across the heterogeneous interface (R_{ct}) coupled to C_3, the total capacitance in the solid phase and the solid-electrolyte interface, which in standard DSCs is a chemical capacitance[30] and is denoted C_μ. A magnified view of the high frequency region, Figure 2b, reveals a small semicircle assigned to the resistance (R_{Pt}) and capacitance (C_{Pt}) of the electrolyte/Pt cathode interface. Finally, a ~45° straight-line element results from the resistance to charge transport (R_{tr}) down the length of the tubes.

The impedance of the transmission line shown in Figure 2 (excluding contributions from series resistances (R_S) and the counter electrode, R_{Pt} and C_{Pt}) is[31,32]

$$Z(\omega) = \left(\frac{R_{tr}R_{ct}}{1 + i\omega/\omega_{rec}}\right)^{1/2} \coth[(R_{tr}/R_{ct})^{1/2}(1 + i\omega/\omega_{rec})^{1/2}] \quad (2)$$

where $\omega_{rec} = (R_{ct}C_3)^{-1}$ is the frequency of the charge-transfer process. Good fits to the equivalent circuit model were obtained at all applied potentials investigated.

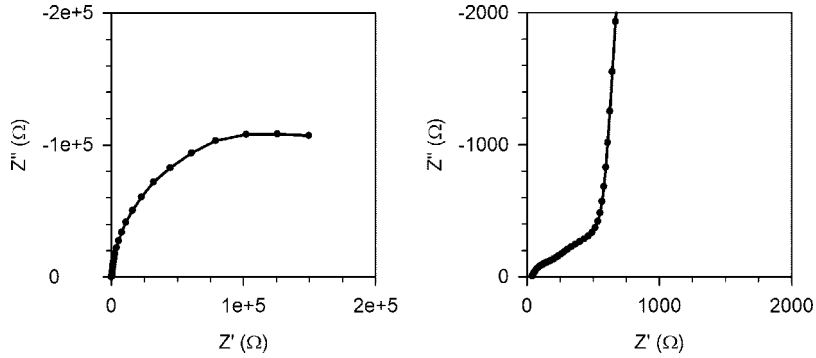

Figure 3. Impedance spectra of representative EIS data at 300 mV forward bias in the dark. Second panel shows 100× magnification of the same spectra to highlight the high-frequency response.

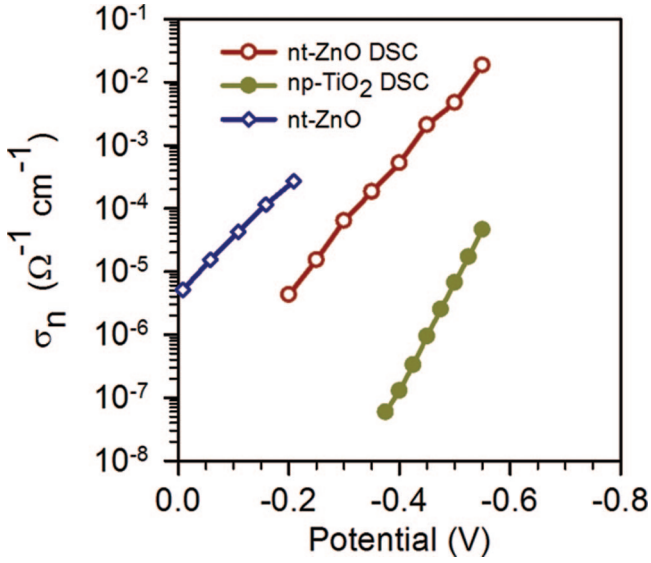

Figure 4. Potential dependence of electron conductivity of unsensitized ZnO nanotube arrays in three-electrode configuration, in ZnO nanotube-based DSC, and in traditional TiO_2 nanoparticle film photoanodes in DSC. Potential scale in inert electrolyte in the three-electrode configuration has been corrected to I_3^-/I^- as a reference.

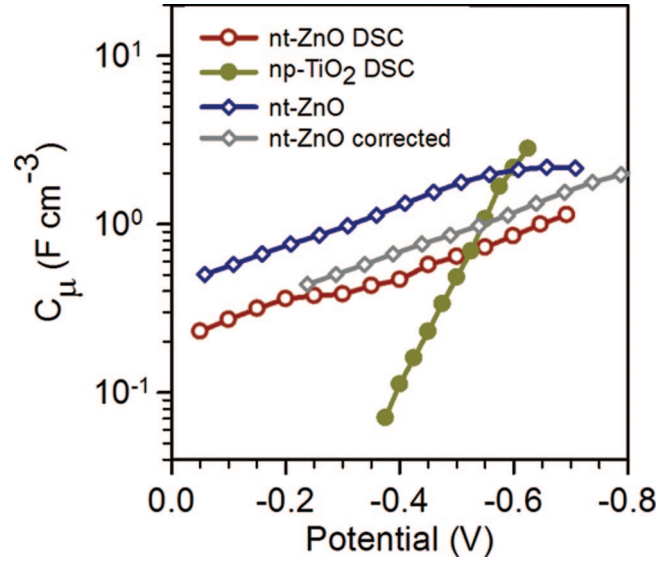

Figure 5. Capacitance of ZnO nanotube array in DSC and three-electrode configuration compared to traditional TiO_2 nanoparticle DSC. The line in gray diamonds is displaced in the horizontal axis to account for a shift of the conduction band as implied by conductivity measurements. Potential scale in inert electrolyte in the three-electrode configuration has been corrected to the I_3^-/I^- reference.

The first parameter studied from the fit of EIS data is the electron conductivity, σ_n, which can be derived according to

$$\sigma_n = \frac{L}{B} R_{tr}^{-1} \tag{3}$$

where R_{tr} is the macroscopic transport resistance, L is the length of the tubes, and B is the projected area of the photoanode exposed through the Suryln frame. The conductivities of ZnO nanotube array (nt-ZnO) and TiO_2 nanoparticles (np-TiO_2) in high efficiency (10% power efficient)[4] based DSCs are compared in Figure 4.

Compared to a traditional np-TiO_2 platform, the polycrystalline nt-ZnO array deposited by ALD shows more than 100 times greater conductivity at equal applied potential, with respect to I^-/I_3^-. This is an important result with respect to photovoltaic performance as it renders the cell tolerant to much faster electron recombination kinetics - at least in terms of sustaining high η_{CC} and IPCE. Furthermore, the dye-free ZnO sample displays even higher conductivity than the ZnO electrode deployed in the DSC configuration. This finding suggests an upward displacement of the conduction band of the 16 nm thick nt-ZnO (ca. 0.15−0.20 eV) due to electrolyte composition and adsorption of dye molecules.[29,33]

Another important aspect of photovoltaic operation is the capacitance at forward bias. According to photovoltaic principles,[3] dye injection under illumination increases the of electron density, n, which raises the quasi-Fermi level, E_F, producing the photovoltage. Since $dE_F = -qdV$, where q is the elementary charge, the relationship of voltage to carrier density in EIS is reflected in a chemical capacitance which has the general form

$$C_\mu = q\frac{dn}{dV} \tag{4}$$

Therefore, we expect the capacitance to increase with forward bias, signifying greater carrier accumulation. For example, for an exponential distribution of states in the bandgap (as is typically observed in np-TiO_2), eq 4 implies that the value of the capacitance goes as[34]

$$C_\mu = C_{0,\mu} \exp\left[-\alpha\frac{qV}{k_B T}\right] \tag{5}$$

where k_BT is the thermal energy and $\alpha = T/T_0$, T_0 being a parameter with temperature units that indicates the depth of the distribution. T_0 values of 800−1200 K[4,34] have typically been found for np-TiO_2. For nt-ZnO photoanodes the capacitance also increases exponentially at forward bias, Figure 5.

The increase of the capacitance indicates that good electrical communication is obtained between the quasi-Fermi level in

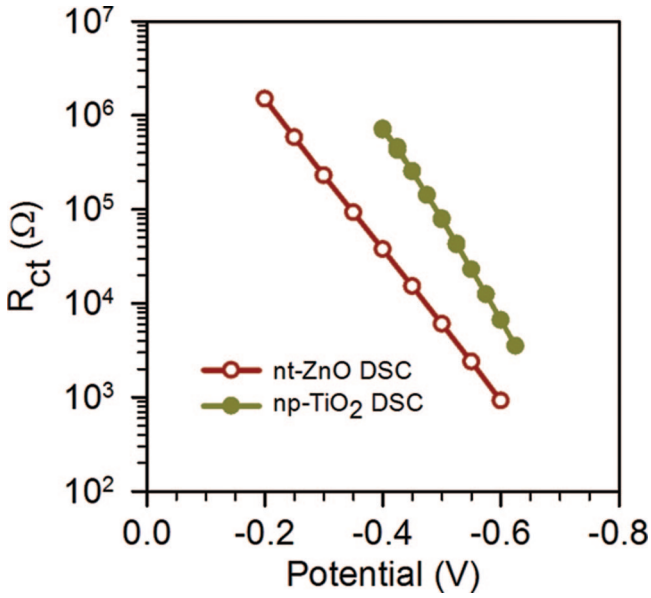

Figure 6. Comparison of R_{ct} value for nt-ZnO DSCs and np-TiO_2 DSCs.

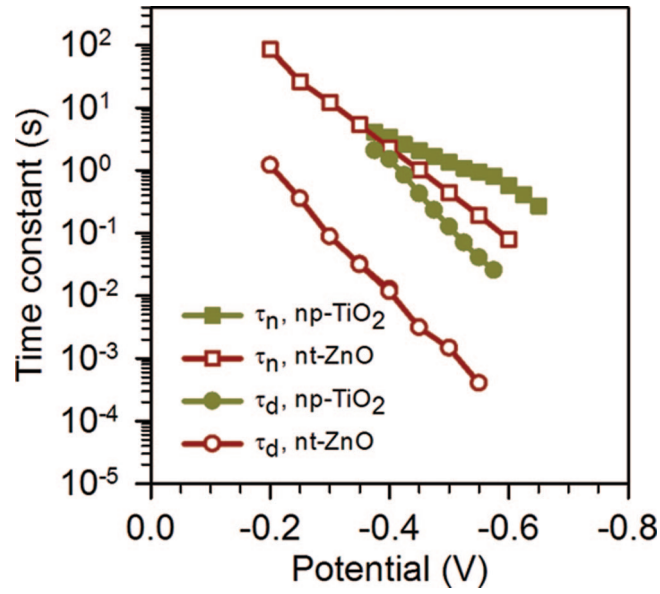

Figure 7. Comparison of charge lifetime (squares) and charge collection time (circles) for the ZnO nanotube array DSC (red, open symbols) and traditional nanoparticle TiO_2 DSC (yellow, closed symbols).

the semiconductor and the conducting substrate. It also shows that there is significant charge accumulation in the ZnO pores walls. The capacitance results present reproducible values of α in both the DSC electrolyte and aqueous solution, indicating that the electronic state distribution remains constant despite the change in surrounding meadia. The nt-ZnO DSC exhibits a smaller capacitance than the unsensitized photoanode measured in inert nonaqueous electrolyte (in the three-electrode configuration). A major part of this difference is explained by a shift of the conduction band as deduced from the conductivity data. Indeed, if the capacitance data are displaced in potential by the same amount seen for as the conductivity, as shown in the gray diamonds in Figure 5, we obtain very similar values of capacitances in the two electrolytes. The small remaining difference may be attributed to the interaction of adsorbed dye molecules with ZnO surface traps. Figure 5 also shows that the slope of the capacitance versus potential plot for nt-ZnO is substantially smaller than typically obtained for np-TiO_2. For nt-ZnO α is 0.06, yielding a $T_0 \sim 5000$ K. Interestingly, similar values of T_0 (5500 K) have recently been reported for TiO_2 nanotube photoanodes.[25,35] Further interpretation of the capacitance of ZnO nanotube arrays is not straightforward, since the active layer is relatively thin and the degree of doping is unknown. For example, one can not fully discard the possibility that a depletion layer is formed in the surface of the ZnO layer as observed in thicker ZnO pillars.[36]

In Figure 3 it may be observed that the charge recombination resistance, R_{ct}, is much larger than the transport resistance—a feature generally necessary for good performance of a DSC.[11] However, the values R_{ct} are smaller for nt-ZnO than for np-TiO_2. Furthermore, the potential dependence of R_{ct} is much weaker for nt-ZnO than for np-TiO_2, Figure 6. The potential dependence can be quantified in terms of the Buttler−Volmer transfer factor (β) via[29]

$$R_{ct} = R_{0,ct} \exp\left[\beta \frac{qV}{k_B T}\right] \quad (6)$$

Application of eq 6 yields $\beta_{ZnO} = 0.46$ and $\beta_{TiO_2} = 0.60$. (Note that the Butler−Volmer equation, originally devised for metal electrodes, is employed here in a phenomenological fashion; the significance and the origin of Butler−Volmer behavior are fundamentally different for semiconductor/solution versus metal/solution interfaces.)

The smaller charge transfer resistance implies that the open circuit potential will be reduced for ZnO. The consequence of the smaller transfer factor for nt-ZnO relative to np-TiO_2 is a smaller fill factor in the nt-ZnO DSC.[37]

It is common to discuss the collection efficiency in terms of the characteristic constants for electron transport (τ_d) and lifetime (τ_n)[38] since these time constants can be also obtained by alternative techniques, such as time transients of intensity modulated photocurrent spectroscopy (IMPS).[39] If the capacitance is taken to be strictly "chemical" in nature (reflecting density of states), it is reasonable to adopt a multiple trapping diffusion interpretation in which $\tau_d = R_{tr}C_\mu = L^2/D_n$ and $\tau_n = R_{ct}C_\mu$ where D_n is the chemical diffusion coefficient.[40] Several features of the nt-ZnO DSC charge dynamics are noteworthy, Figure 7. First, we observe a linear and roughly parallel trend in τ_n and τ_d with increasing applied potential. Furthermore, τ_d is more than 2 orders of magnitude shorter than τ_n at all measured potentials ($R_{tr} \ll R_{ct}$ always, as in Figure 3). Given the favorable competition between τ_n and τ_d shown in Figure 7, we expect η_{CC} to be excellent, as will be demonstrated in section C.

A striking feature in Figure 7 is the transit time of electrons in the nt-ZnO array, which is dramatically shorter (almost 2 orders of magnitude) than for np-TiO_2 despite the fact that the electron transport distance is ~4 times longer for nt-ZnO tubes. Equally important is the relatively small difference in τ_n values for the two photonanodes, while the difference in τ_d is in large contrast. Slopes for charge lifetime (log of τ_n vs potential) are significantly different due to the differences in slopes of C_μ and R_{ct}, while the slopes of τ_d for the two photoanodes are quite similar.

The factor governing η_{CC} is the effective diffusion length, L_n, that may be calculated from[40]

$$L_n = \sqrt{D_n \tau_n} = L\sqrt{\frac{\tau_n}{\tau_d}} = L\sqrt{\frac{R_{ct}}{R_{tr}}} \quad (7)$$

L_n will exceed the photoanode thickness, L, when $\tau_d < \tau_n$ ($R_{tr} < R_{ct}$). From Figure 3 it is clear that $R_{ct} \gg R_{tr}$, suggesting

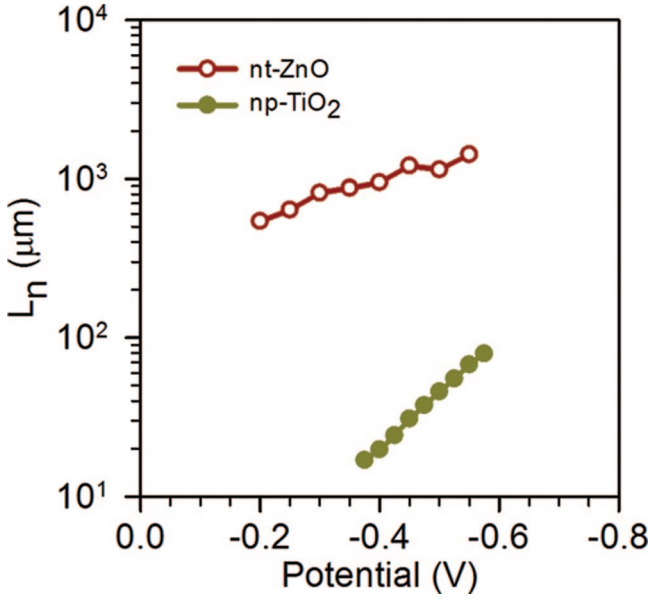

Figure 8. Effective diffusion length in completed ZnO nanotubes array DSC compared to an efficient nanoparticle TiO_2 DSC. The diffusion length of the ZnO-based DSC exceeds the tubes' length by more than 1 order of magnitude.

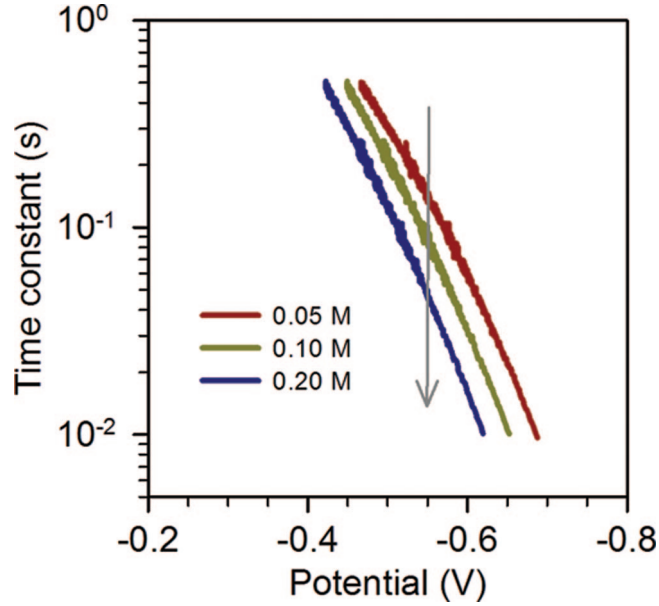

Figure 9. Electron lifetime in DSCs with increasing concentration of I_3^-. The gray arrow illustrates the decrease in electron lifetime (at equal potential) with increasing $[I_3^-]$.

a good η_{CC}. Using the aforementioned values obtained from EIS, we find that charges may be extracted from tubes up to ~1 mm in length, Figure 8. The 100× shorter electron transit time produces an extremely long diffusion length that allows charge collection over the entirety of the exceptionally thick (64 μm) photoanode.

The observation that electrons are extracted efficiently over the full tube length suggests that increasing the roughness factor (here ~400) to values of the order of np-TiO_2 films (>1000) will not reduce η_{CC}. In addition, the use of redox solutions that induce shorter electron lifetimes (due to faster kinetics for electron interception) may be feasible without loss of η_{CC}. Among the attractions of alternative redox couples may be more favorable redox potentials, higher transparency and/or less tendency to cause corrosion. It is important to understand, as indicated by eq 7, that the efficacy of charge collection is dependent upon the *ratio* of resistances for transport (small R_{tr}) and recombination (large R_{ct}), not their absolute magnitudes.

Calculation from the aforementioned relationship $\tau_d = L^2/D_n$ allows one to estimate a lower limit of the diffusion coefficient of electrons in the conduction band of 0.4 $cm^2\ s^{-1}$ for a nt-ZnO DSC. This value exceeds by ~1000 times the largest values previously reported for DSC photoanodes.[4,41] The plausibility of this value may be weighed against the theoretically predicted diffusion coefficient for polycrystalline ZnO. Equation 7 can also be expressed as[41]

$$\frac{D_n}{\mu_n} = \chi_n \frac{k_B T}{q} \tag{8}$$

where μ_n represents mobility ($cm^2\ V^{-1}\ s^{-1}$) and χ_n is a thermodynamic factor that for the exponential distribution takes the value α^{-1}; therefore

$$D_n = \frac{k_B T_0}{q} \mu_n \tag{9}$$

The measured value of μ_n for similarly prepared polycrystalline ZnO films grown by ALD before firing is ~15 to 17 $cm^2\ V^{-1}\ s^{-1}$; this is roughly 1 order of magnitude lower than the accepted single crystal value of 180 $cm^2\ V^{-1}\ s^{-1}$.[42,43] Therefore, the expected limiting value for D_n will be 7 $cm^2\ s^{-1}$. The maximum value here, D_n= 0.4 cm^2/s^{-1}, suggests that diffusion is still limited by traps and thus that the Fermi level has not reached the conduction band. A second useful point of reference is the estimated diffusion coefficient (0.05 to 0.5 cm^2/s^{-1}) of a single dry, ZnO nanowire removed from an array grown by aqueous chemistry.[10] Given this range, the D_n derived from EIS analysis in a fired and completed nt-ZnO DSC (0.4 $cm^2\ s^{-1}$) is not unreasonable. Nonetheless, given the uncertainty about the nature of the measured capacitance, this interpretation must be regarded as preliminary, since in the case of depletion capacitance, D_n and μ_n cannot be derived by this procedure and must be extracted directly from the conductivity (and knowledge of the carrier number).

B. Photovoltage Decay. Regardless of mechanism, it is clear that electrons are extracted more rapidly and over greater distance than electrons in traditional np-TiO_2 photanodes. Since electron transport is significantly faster in ZnO nanotube array photoanodes, we expect the device to be more tolerant to "faster" redox shuttles. That is, we expect similar J_{SC} even upon intentional acceleration of the rate of electron interception (decreasing R_{ct}), up to the point at which at which $\tau_n \approx \tau_d$. This hypothesis has been tested on nt-ZnO based DSC by systematically increasing the concentration of the hole shuttle, I_3^- (an experimentally convenient alternative to investigating directly, intrinsically faster redox shuttles). Here, open-circuit photovoltage decay measurements were used in place of EIS in order to more quickly screen the range of τ_n.[44] As expected, τ_n becomes shorter with increasing $[I_3^-]$, Figure 9.

C. Incident-Photon-to-Current Efficiencies. In order to corroborate the EIS estimation of L_n, the η_{CC} of nt-ZnO DSC may be probed (to a first approximation) by analysis of monochromatic IPCEs. Since monochromatic IPCEs are a function of at least three distinct microscopic processes (eq 1), it is necessary to deconvolute in order to understand the competition between electron extraction and interception. While the η_{LH} of these photoanodes is not trivial to quantify owing to their scattering nature, in principle it may be estimated by employing an integrating sphere or by subtracting the scattering

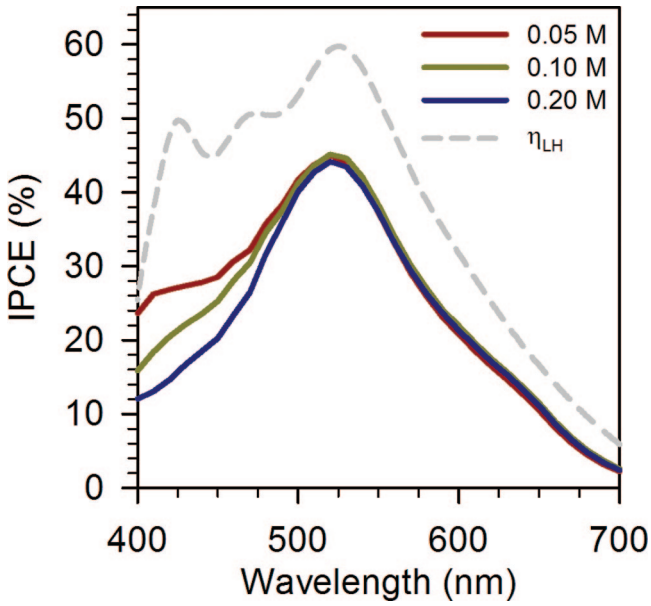

Figure 10. Incident photon to current efficiencies for nt-ZnO DSCs with increasing $[I_3^-]$. For reference, the dashed line shows the η_{LH} of the dye on a representative ZnO nanotubes array.

from a membrane prior to dye loading. Regardless, relative changes in the other two variables (η_{CS} and η_{CC}) may be probed by simply holding η_{LH} (and the incident light) constant. That is, if a nominally identical photoanode is employed, any change in the IPCE must be due to changes in η_{CS} and/or η_{CC}. The same can be said for η_{CS}, which has not been quantified for these DSC but is expected to remain constant for identically prepared photoanodes in contact with similar redox solutions. Thus, a relative measure of the remaining variable of interest, η_{CC}, is reported by the magnitude of the IPCE. That values for η_{CC} are approximately equal for the various iodide-based electrolytes is illustrated in Figure 10. The differences observed at low wavelengths are due to the competitive absorbance of the redox couple when the I_3^- concentration is increased.

As is often the case for ZnO-based DSCs, the peak IPCE does not reach unity. This is likely due to a combination of the poor dye loading characteristics of ZnO[45,46] and the modest η_{LH} (~60% at the peak) of nanotube photoanodes prepared on commercially available AAO templates. At wavelengths <500 nm the photoresponse is further reduced under high $[I_3^-]$ due to light attenuation by the concentrated shuttle, which absorbs strongly in this region. Most importantly, at wavelengths >500 nm the IPCE values with the varying iodide-based shuttle solutions are nearly identical. That the values are not reduced upon concentration of the I_3^- suggests η_{CC} is ~1 in each case. Thus, certainly under standard electrolyte conditions and even upon twice doubling the I_3^- concentration, electrons are collected over a distance ~4 times greater than in the most efficient DSC to date.[4] As indicated above, we expect electrons to be extractable from tubes as great ~1 mm in length.

Conclusions

The effective diffusion coefficient for electron in ZnO nanotube array photoanodes is measured to be 3 orders of magnitude greater than in any DSC photoanode reported to date. Photovoltage decay measurements and analysis of IPCEs with increasing $[I_3^-]$ are consistent with the values of τ_n and τ_d as derived from electrochemical impedance spectroscopy. Despite the relatively large length of the tubes constituting the photoanode (64 μm), electrons are efficiently and rapidly extracted from throughout the anode. In addition, we anticipate that efficient charge collection will be feasible in nt-ZnO DSCs that employ redox couples other than $I_3^-I^-$.

Acknowledgment. We dedicate this paper to our friend and Colleague George Schatz on the occasion of his 60th birthday. The work at Northwestern is supported by the U.S. Department of Energy, Basic Energy Sciences Program, under Grant No. DE-FG02-87ER13808. Work at Argonne is supported by the U.S. Department of Energy, BES-Materials Sciences, under Contract No. W-31-109-ENG-38. Work at Universitat Jaume I is supported by Ministerio de Ciencia e Innovación under Project Nos. MAT2007-62982 and HOPE CSD2007-00007 (Consolider-Ingenio 2010). M.S.G. thanks CNPq - Brasil for the fellowship (201516/2007-1).

References and Notes

(1) Nazeeruddin, M. K.; Kay, A.; Rodicio, I.; Humphrybaker, R.; Muller, E.; Liska, P.; Vlachopoulos, N.; Gratzel, M. *J. Am. Chem. Soc.* **1993**, *115*, 6382–6390.
(2) O'Regan, B.; Gratzel, M. *Nature* **1991**, *353*, 737–740.
(3) Bisquert, J.; Cahen, D.; Hodes, G.; Ruhle, S.; Zaban, A. *J. Phys. Chem. B* **2004**, *108*, 8106–8118.
(4) Wang, Q.; Ito, S.; Gratzel, M.; Fabregat-Santiago, F.; Mora-Sero, I.; Bisquert, J.; Bessho, T.; Imai, H. *J. Phys. Chem. B* **2006**, *110*, 25210–25221.
(5) Kayes, B. M.; Atwater, H. A.; Lewis, N. S. *J. Appl. Phys.* **2005**, 97.
(6) Li, G.; Shrotriya, V.; Huang, J. S.; Yao, Y.; Moriarty, T.; Emery, K.; Yang, Y. *Nat. Mater.* **2005**, *4*, 864–868.
(7) Sodergren, S.; Hagfeldt, A.; Olsson, J.; Lindquist, S. E. *J. Phys. Chem.* **1994**, *98*, 5552–5556.
(8) Martinson, A. B. F.; Hamann, T. W.; Pellin, M. J.; Hupp, J. T. *Chem.—Eur. J.* **2008**, *14*, 4458–4467.
(9) Lee, J. J.; Coia, G. M.; Lewis, N. S. *J. Phys. Chem. B* **2004**, *108*, 5282–5293.
(10) Law, M.; Greene, L. E.; Johnson, J. C.; Saykally, R.; Yang, P. D. *Nat. Mater.* **2005**, *4*, 455–459.
(11) Martinson, A. B. F.; Elam, J. W.; Hupp, J. T.; Pellin, M. J. *Nano Lett.* **2007**, *7*, 2183–2187.
(12) Ku, C. H.; Wua, J. J. *Appl. Phys. Lett.* **2007**, 91.
(13) Galoppini, E.; Rochford, J.; Chen, H. H.; Saraf, G.; Lu, Y. C.; Hagfeldt, A.; Boschloo, G. *J. Phys. Chem. B* **2006**, *110*, 16159–16161.
(14) Greene, L. E.; Yuhas, B. D.; Law, M.; Zitoun, D.; Yang, P. D. *Inorg. Chem.* **2006**, *45*, 7535–7543.
(15) Macák, J. M.; Tsuchiya, H.; Ghicov, A.; Schmuki, P. *Electrochem. Commun.* **2005**, *7*, 1133–1137.
(16) Law, M.; Greene, L. E.; Radenovic, A.; Kuykendall, T.; Liphardt, J.; Yang, P. D. *J. Phys. Chem. B* **2006**, *110*, 22652–22663.
(17) Elam, J. W.; Martinson, A. B. F.; Pellin, M. J.; Hupp, J. T. *Chem. Mater.* **2006**, *18*, 3571–3578.
(18) Elam, J. W.; Baker, D. A.; Hryn, A. J.; Martinson, A. B. F.; Pellin, M. J.; Hupp, J. T. *J. Vac. Sci. Technol. A* **2008**, *26*, 244–252.
(19) Elam, J. W.; Baker, D. A.; Martinson, A. B. F.; Pellin, M. J.; Hupp, J. T. *J. Phys. Chem. C* **2008**, *112*, 1938–1945.
(20) Hamann, T. W.; Martinson, A. B. E.; Elam, J. W.; Pellin, M. J.; Hupp, J. T. *Adv. Mater.* **2008**, *20*, 1560–1564.
(21) Hamann, T. W.; Martinson, A. B. F.; Elam, J. W.; Pellin, M. J.; Hupp, J. T. *J. Phys. Chem. C* **2008**, *112*, 10303–10307.
(22) Pellin, M. J.; Elam, J. W.; Libera, J. A.; Martinson, A. B. F.; Hupp, J. T. *ECS Trans.* **2007**, *3*, 243–246.
(23) Martinson, A. B. F.; Elam, J. W.; Liu, J.; Pellin, M. J.; Marks, T. J.; Hupp, J. T. *Nano Lett.* **2008**, *8*, 2862–2866.
(24) Hamann, T. W.; Jensen, R. A.; Martinson, A. B. F.; Ryswyk, H. V.; Hupp, J. T. *Energy Environ. Sci.* **2008**, *1*, 66–78.
(25) Fabregat-Santiago, F.; Barea, E. M.; Bisquert, J.; Mor, G. K.; Shankar, K.; Grimes, C. A. *J. Am. Chem. Soc.* **2008**, *130*, 11312–11316.
(26) Fabregat-Santiago, F.; Garcia-Belmonte, G.; Bisquert, J.; Zaban, A.; Salvador, P. *J. Phys. Chem. B* **2002**, *106*, 334–339.
(27) Kern, R.; Sastrawan, R.; Ferber, J.; Stangl, R.; Luther, J. *Electrochim. Acta* **2002**, *47*, 4213–4225.
(28) Bisquert, J.; Vikhrenko, V. S. *J. Phys. Chem. B* **2004**, *108*, 2313–2322.
(29) Fabregat-Santiago, F.; Bisquert, J.; Garcia-Belmonte, G.; Boschloo, G.; Hagfeldt, A. *Sol. Energy Mater. Sol. Cells* **2005**, *87*, 117–131.
(30) Bisquert, J. *Phys. Chem. Chem. Phys.* **2003**, *5*, 5360.

(31) Bisquert, J.; Garcia-Belmonte, G.; Fabregat-Santiago, F.; Ferriols, N. S.; Bogdanoff, P.; Pereira, E. C. *J. Phys. Chem. B* **2000**, *104*, 2287–2298.
(32) Bisquert, J. *J. Phys. Chem. B* **2002**, *106*, 325–333.
(33) Haque, S. A.; Palomares, E.; Cho, B. M.; Green, A. N. M.; Hirata, N.; Klug, D. R.; Durrant, J. R. *J. Am. Chem. Soc.* **2005**, *127*, 3456–3462.
(34) Bisquert, J.; Fabregat-Santiago, F.; Mora-Sero, I.; Garcia-Belmonte, G.; Barea, E. M.; Palomares, E. *Inorg. Chim. Acta* **2008**, *361*, 684–698.
(35) Jennings, J. R.; Ghicov, A.; Peter, L. M.; Schmuki, P.; Walker, A. B. *J. Am. Chem. Soc.* **2008**, *130*, 13364–13372.
(36) Mora-Sero, I.; Fabregat-Santiago, F.; Denier, B.; Bisquert, J.; Tena-Zaera, R.; Elias, J.; Levy-Clement, C. *Appl. Phys. Lett.* **2006**, *89*, 3.
(37) Fabregat-Santiago, F.; Bisquert, J.; Palomares, E.; Otero, L.; Kuang, D. B.; Zakeeruddin, S. M.; Gratzel, M. *J. Phys. Chem. C* **2007**, *111*, 6550–6560.
(38) Bisquert, J.; Vikhrenko, V. S. *J. Phys. Chem. B* **2004**, *108*, 2313–2322.
(39) Dloczik, L.; Ileperuma, O.; Lauermann, I.; Peter, L. M.; Ponomarev, E. A.; Redmond, G.; Shaw, N. J.; Uhlendorf, I. *J. Phys. Chem. B* **1997**, *101*, 10281–10289.
(40) Bisquert, J. *J. Phys. Chem. B* **2002**, *106*, 325–333.
(41) Bisquert, J. *Phys. Chem. Chem. Phys.* **2008**, *10*, 3175–3194.
(42) Lim, S. J.; Kwon, S. J.; Kim, H. *Thin Solid Films* **2008**, *516*, 1523–1528.
(43) Huby, N.; Ferrari, S.; Guziewicz, E.; Godlewski, M.; Osinniy, V. *Appl. Phys. Lett.* **2008**, 92.
(44) Zaban, A.; Greenshtein, M.; Bisquert, J. *ChemPhysChem* **2003**, *4*, 859–864.
(45) Bauer, C.; Boschloo, G.; Mukhtar, E.; Hagfeldt, A. *J. Phys. Chem. B* **2001**, *105*, 5585–5588.
(46) Chou, T. P.; Zhang, Q.; Cao, G. *J. Phys. Chem. C* **2007**, *111*, 18804–18811.

JP810406Q